J. Quant. Spectrosc. Radiat. Transfer Vol. 49, No. 6, pp. 599–607, 1993
Printed in Great Britain. All rights reserved

0022-4073/93 $6.00 + 0.00
Copyright © 1993 Pergamon Press Ltd

BOUNDARY LAYER STRATUS CLOUDS: INFERRED FROM SATELLITE INFRARED SPECTRAL MEASUREMENTS OVER OCEANS

C. PRABHAKARA,†‡ J.-M. YOO,§ D. P. KRATZ,¶ and G. DALU‖

†Laboratory for Atmospheres, NASA/GSFC Greenbelt, MD 20771, U.S.A., §Applied Research Corporation, Landover, MD 20785, U.S.A., ¶Lockheed Engineering & Sciences Company, Hampton, VA 23666, U.S.A., and ‖CNR, Area Della Ricerca Di Cagliari, Itali

(Received 28 September 1992)

Abstract—A method to remotely sense marine stratus clouds, that are underneath the boundary layer inversion produced by strong subsidence, is developed with the help of the measurements made by the Infrared Interferometer Spectrometer (IRIS) on board the *Nimbus 4* satellite. These measurements, which had a spectral resolution of 2.8 cm^{-1} and a field view of ~100 km in the region 870–980 cm^{-1}, allow one to compare the weak absorption due to water vapor lines with that of the weak ν_3–ν_1 band of CO_2. From such a comparison it is possible to sense the presence of these boundary layer stratus clouds. Maps of these clouds over subsidence regions of the tropical and subtropical oceans deduced from IRIS data show the usefulness of the technique to climatological studies.

INTRODUCTION

Low altitude stratus clouds play an important role in the radiation energy balance of the ocean–atmosphere system.[1,2] Since these clouds can reflect shortwave solar radiation efficiently and also radiate to space at relatively warm temperature, they can lead to a cooling. These clouds are largely present over the regions of the tropics and subtropics where large scale subsidence exists. Remote sensing of these clouds can be valuable in studies of climate and global change.

At the present time, satellite-based cloud studies depend quite heavily on high spatial resolution (~1–10 km) data such as that provided by AVHRR or *Nimbus 7*-THIR.[3–5] Such analyses attempt to take advantage of the details in the spatial distribution of satellite data to derive cloud information. Unlike these methods the objective of this study is to utilize the infrared (i.r.) spectral information for discerning the boundary layer stratus cloud type prevailing in a large field of view, typically ~100 km in size. Since clouds are complex phenomena over the globe, it is desirable to take a different remote sensing approach to study them.

SPECTRAL INFORMATION IN THE 870–980 cm^{-1}

Liquid drops or ice particles in clouds produce broad band features in the i.r. region.[6,7] For this reason it is preferable to study the cloud properties with the help of their broad i.r. features in the spectral region where there is minimal interference from strong absorption due to the atmospheric gases, i.e. CO_2, H_2O, O_3, N_2O and CH_4. The window region between 10 and 13 μm suits this purpose well. In our earlier studies,[8,9] thin high altitude cirrus clouds, associated with the spreading anvils of deep convective clouds, were investigated utilizing such broad band i.r. extinction properties in the window region based on the *Nimbus 4* Infrared Interferometer Spectrometer (IRIS) data. Here we are exploring the low altitude boundary layer stratus clouds with the help of these data taking advantage of the 2.8 cm^{-1} resolution. Since the temperature of the boundary layer stratus differs from the sea surface temperature by only 10–15 K the extinction features in the i.r. spectrum introduced by such clouds will be considerably weak compared to that of high

‡To whom all correspondence should be addressed.

altitude clouds. For this reason we are considering here the spectral feature, at 2.8 cm^{-1} resolution, of the water vapor and a weak band of CO_2 in the window region that are influenced in a characteristic manner in response to the existence of the boundary layer stratus.

At 2.8 cm^{-1} resolution the fine structure of the lines of water vapor and CO_2 is not apparent. Nevertheless, we can still observe some spectral structure at this resolution which is sufficient for our study. A clear sky i.r. spectrum obtained by IRIS over tropical Pacific ocean is shown in Fig. 1 to indicate the nature of these data. The strong absorption bands of water vapor, CO_2, O_3, N_2 and CH_4 may easily be noticed in Fig. 1. In the window region between 10 and 13 μm there are a few weak water vapor lines and some weak spectral features of CO_2. A weak band (hot band) of CO_2, ν_3–ν_1 band, occurs in the region 930–980 cm^{-1}. As in the case of most molecular absorption bands pressure broadening of spectral lines increases absorption in this band. In addition, due to the nature of the energy transitions that produce this CO_2 band, the absorption increases sharply as temperature increases. For these reasons CO_2 absorption in this weak band increases rapidly toward the sea surface as the pressure and temperature increase.

The transmission from surface to the top of the atmosphere for the spectral region 870–980 cm^{-1}, computed with a detailed line-by-line model,[10] is shown in Fig. 2 to illustrate the spectral features of (a) 'hot' band of CO_2, and (b) the water vapor lines. For simplicity, absorption due to the continuum of water vapor and weak absorption due to O_3 are not included in this illustration. In the region *A*, i.e. 870–930 cm^{-1}, mainly water vapor lines are present. At 2.8 cm^{-1} resolution we note in region *B*, i.e. 930–980 cm^{-1}, the spectral features of the hot band coincide closely with the water vapor lines. Further it may be noticed that the water vapor lines in *A* are much stronger

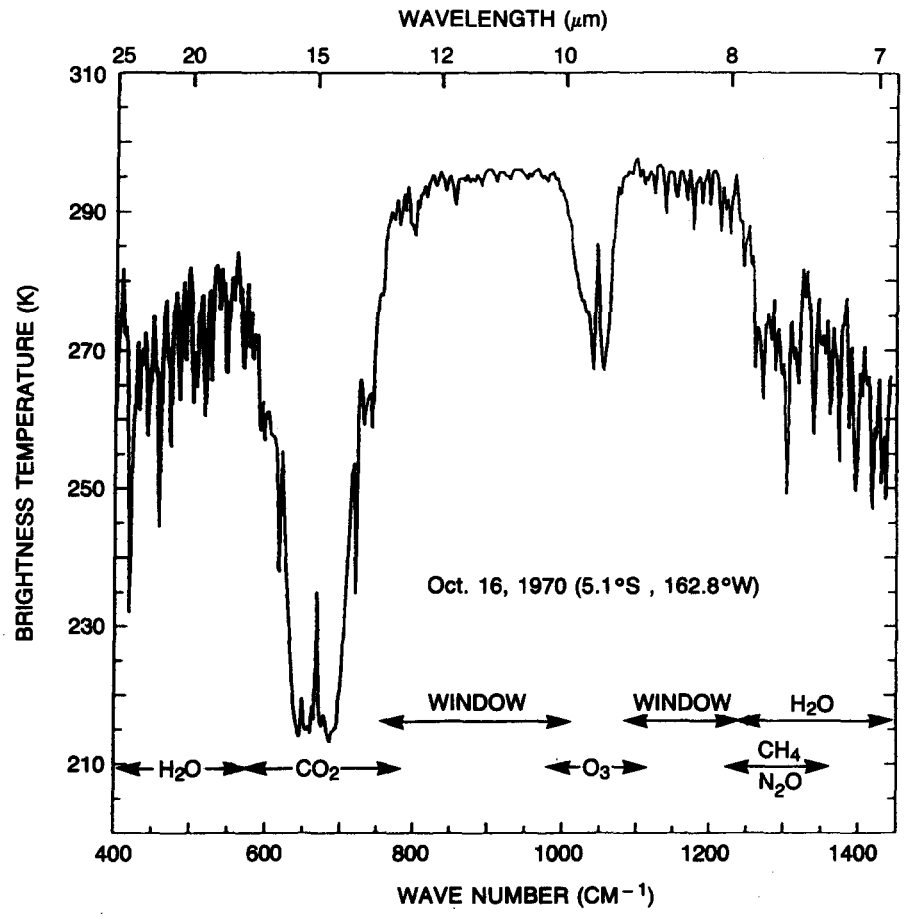

Fig. 1. Clear sky tropical ocean brightness temperature spectrum measured by *Nimbus 4* IRIS. Spectral resolution is 2.8 cm^{-1} and the field of view is 100 km. Spectral features of CO_2, O_3, H_2O, N_2O and CH_4 are identified.

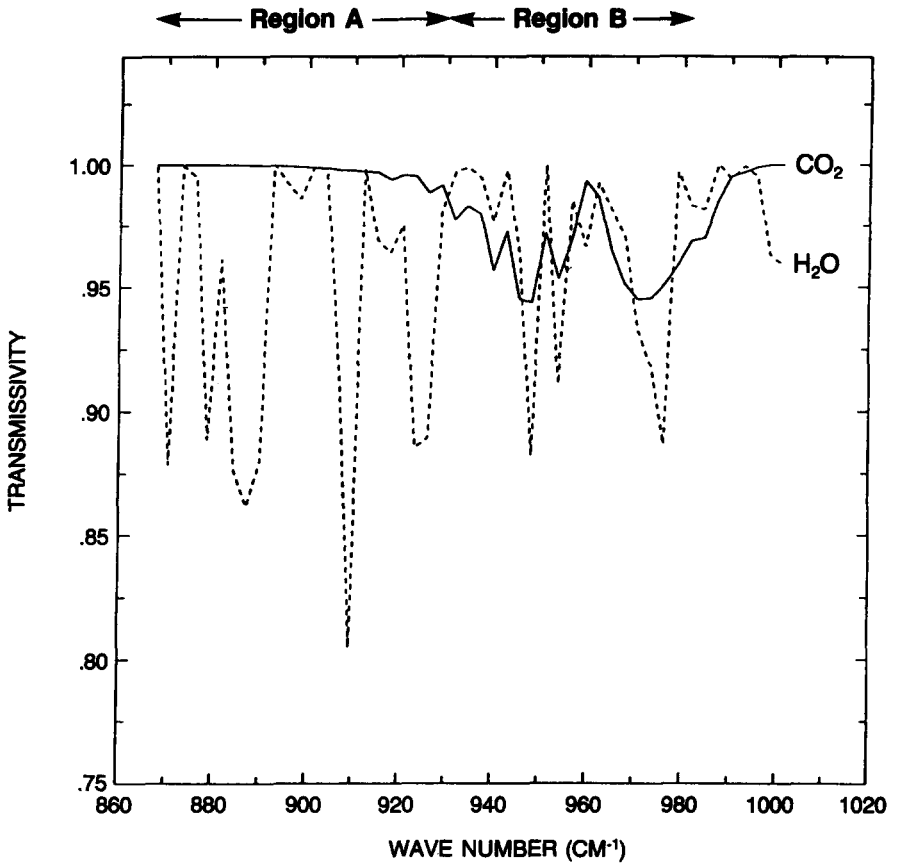

Fig. 2. Spectral transmission from 1000 mbar to top of the atmosphere in the 860–1000 cm^{-1} due to CO_2 (—) and H_2O (– – –) computed with a 'line by line' model and averaged to 2.8 cm^{-1} resolution. The region *A* (870–930 cm^{-1}) and the region *B* (930–980 cm^{-1}) are shown to discriminate water vapor and CO_2 absorption.

than the water vapor lines in *B*. We note in Fig. 2 that at 2.8 cm^{-1} resolution the 'hot' band of CO_2 produces a maximum absorption of only 5% near 948 and 976 cm^{-1} in region *B*. Water vapor lines that overlap with this CO_2 band can easily eclipse this band. For example, there is an absorption of $\sim$10% in the line centers near 948, 954, and 976 cm^{-1} when the total water vapor content in the atmosphere is 1.5 g/cm^2 (Fig. 2). In comparison to region *B* let us note that, for the same amount of water vapor, absorption in the water vapor lines close to 872, 887 and 909 cm^{-1} in region *A* is $\sim$15%. When the water vapor content in the atmosphere is substantially reduced, the combined spectral absorption due to CO_2 and H_2O in region *B* can exceed that due to water vapor in region *A*.

Water vapor in the atmosphere is markedly reduced by subsidence in the atmosphere which generally produces an inversion over the boundary layer and a stratiform cloud at the base of the inversion (see Fig. 3). Therefore, by comparing the spectral information in region *B* with that in region *A*, we can draw some inferences pertaining to the inversion related stratus clouds over oceans.

THEORETICAL CONSIDERATION

The weak CO_2 absorption band in the 930–980 cm^{-1} region, produces spectral features near 954 and 976 cm^{-1} that respond sharply to the thermal structure of the lower layers of the atmosphere because of strong temperature dependence. This is illustrated in Fig. 4(a) by means of the weighting function, i.e. the derivative of the transmittance τ with respect to altitude for the CO_2 at these two frequencies. For comparison in Fig. 4(b) the weighting function for water vapor at these two

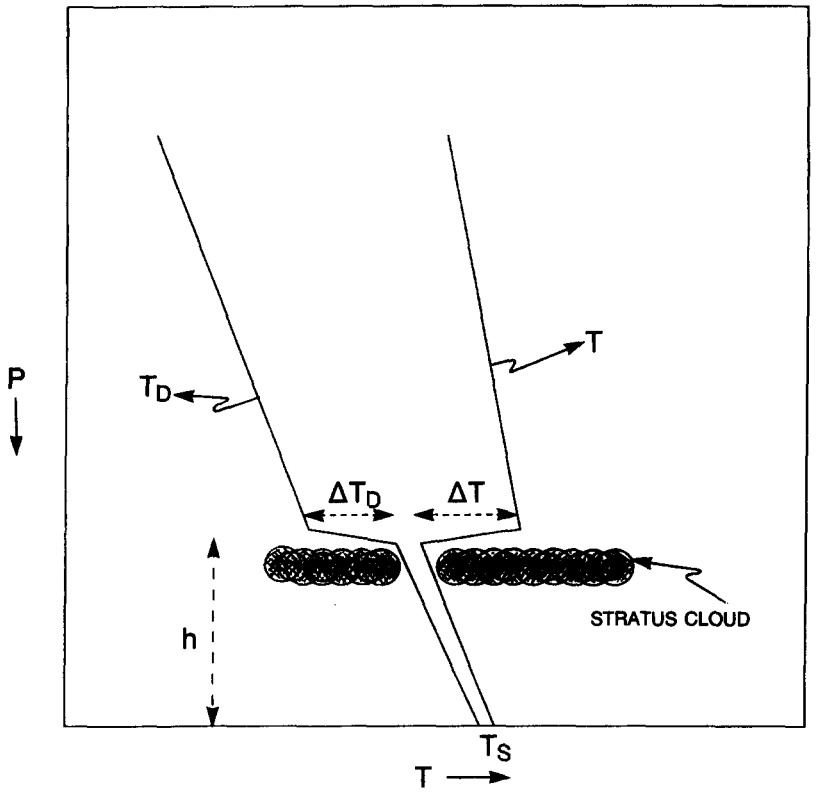

Fig. 3. Schematic figure of the marine boundary layer with an inversion and stratus clouds. T_s is surface temperature, T_D is dew point temperature, h is the height of the inversion base.

frequencies is shown. From Figs 4(a) and 4(b) we note the CO_2 and water vapor weighting functions are similar in their vertical distribution giving the largest weight to the lowest layers of the atmosphere.

Now a simple theoretical analysis can be done to compare the strength of the CO_2 spectral features with that of the water vapor line features in the spectral regions A and B shown in Fig. 2.

In region A water vapor absorption centers are present near 872, 887, and 909 cm^{-1} and there is only weak absorption in the adjacent narrow window regions close to 874, 901, and 916 cm^{-1} (Table 1). From IRIS observations of the radiance at these spectral positions we can determine the mean brightness temperature $\bar{T}_C$ corresponding to the three water vapor absorption centers, and the mean brightness temperature $\bar{T}_W$ from three narrow windows. Then we can express the mean strength of the water vapor lines in the spectral region A as

$$(\delta T)_A = \bar{T}_W - \bar{T}_C, \tag{1}$$

We may note $\bar{T}_W$ is close to the surface temperature in a clear sky condition. Similarly mean strength of the spectral features in the region B can be evaluated from the IRIS data to obtain $(\delta T)_B$. Here absorption is strong near 948, 954, and 976 cm^{-1}, and narrow windows are present near 936, 951, and 961 cm^{-1} (Table 1). Obviously the measured $(\delta T)_B$ contains information on the weak CO_2 band and the overlapping water vapor lines. The magnitude of $(\delta T)_A$ and $(\delta T)_B$ is estimated as follows.

From the equation of radiative transfer we have the intensity I_ν at a wavenumber ν given by

$$I_\nu = B_\nu(T_s)\tau_\nu(p_s) + \int_{\tau_\nu(p_s)}^{1} B_\nu\{T(p)\}\mathrm{d}\tau_\nu(p), \tag{2}$$

where B_ν is Planck's function. τ_ν is the transmittance from a given pressure p in the atmosphere to the radiometer located at the top. p_s and T_s are the surface pressure and temperature,

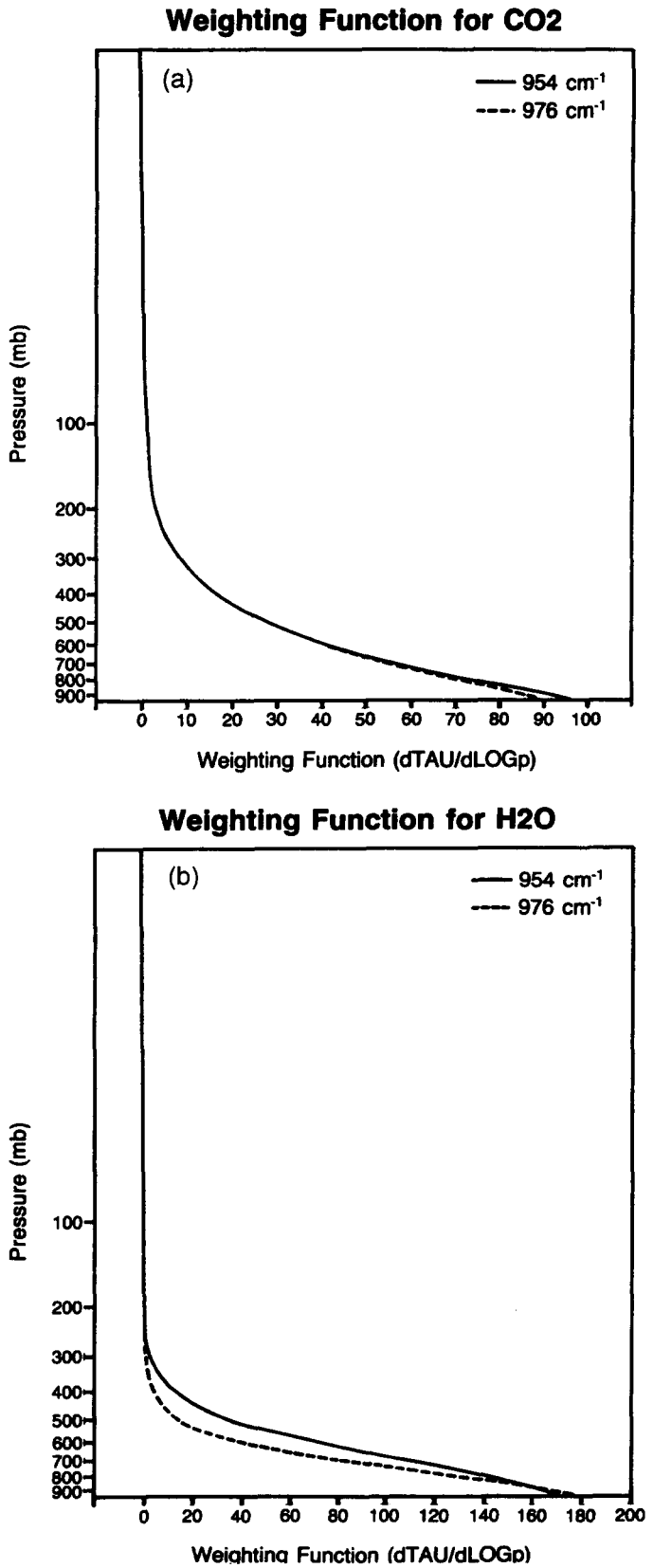

Fig. 4. Weighting function $d\tau/d\log p$ (in arbitrary units) for (a) CO_2, and (b) H_2O (total water vapor content = 1.5 g/cm^2). The two curves correspond to 2.8 cm^{-1} wide spectral intervals at 954 and 976 cm^{-1} respectively. Water vapor continuum absorption is not included.

Table 1. Absorption centers and windows adopted for Regions A and B.

	Region A cm^{-1}			Region B cm^{-1}		
Absorption center	872	887	909	948	954	976
Window	874	901	916	936	951	961
Absorbing gas	H_2O	H_2O	H_2O	H_2O & CO_2	H_2O & CO_2	H_2O & CO_2

respectively, and T is the temperature in the atmosphere. The integral in Eq. (2) may be approximated to give

$$I_\nu = B_\nu(T_s)\tau_\nu(p_s) + B_\nu(\bar{T})\{1 - \tau_\nu(p_s)\} \tag{3}$$

where $\bar{T}$ represents the effective emission temperature of the atmosphere at the wavenumber ν. $\bar{T}$ is given by

$$B(\bar{T}) = \frac{\int_{\tau_\nu(p_s)}^{1} B\{T(p)\}\mathrm{d}\tau_\nu(p)}{\int_{\tau_\nu(p_s)}^{1} \mathrm{d}\tau_\nu(p)}. \tag{4}$$

Now, assuming the transmittance in narrow windows of region A and B to be close to unity, we can express δI the increment in intensity between the center and the adjacent window for each absorption line as

$$\delta I \simeq B(T_s) - [B(T_s)\tau(p_s) + B(\bar{T})\{1 - \tau(p_s)\}] \tag{5}$$

From such estimates of δI for individual spectral features in the regions A and B we can obtain their mean $(\delta I)_A$ and $(\delta I)_B$. With the approximation that the Planck function is linear over a short range in temperatures and wavenumbers we can write

$$(\delta I)_A = C(\delta T)_A \simeq [\{B(T_s) - B(\bar{T})\}\{1 - \tau(p_s)\}]_A \tag{6}$$

and

$$(\delta I)_B = C(\delta T)_B \simeq [\{B(T_s) - B(\bar{T})\}\{1 - \tau(p_s)\}]_B \tag{7}$$

where C is constant of proportionality.

The terms $[1 - \tau(p_s)]_A$ and $[1 - \tau(p_s)]_B$ in the above equations represent the mean absorption of the spectral features in the regions A and B respectively. Furthermore we should note $[1 - \tau(p_s)]_B$ is made up of two absorptions, (a) due to water vapor and (b) due to CO_2. These two weak absorptions add linearly in region B (Fig. 2).

When there is normal temperature and water vapor distribution in the atmosphere we may take $\bar{T}$ in the above equations to be nearly the same for regions A and B, and also for CO_2 and water vapor. This approximation is based on the similarity of the weighting functions for CO_2 and H_2O, as shown in Fig. 4, in the absence of a boundary layer inversion. This leads us to infer that since absorption in water vapor lines is stronger in region A than in region B we will find $(\delta T)_A$ is greater than $(\delta T)_B$ over most of the oceanic regions having normal temperature and water vapor distributions. In fact we find from IRIS observations over regions of the oceans where boundary layer subsidence inversion is generally not present $(\delta T)_A$ is greater than $(\delta T)_B$.

In contrast, when there is an inversion in the boundary layer, produced by strong subsidence motion, the temperature and water vapor profiles are markedly affected. This is illustrated in Fig. 3, which is a schematic diagram of the vertical distribution of wet and dry bulb temperature in the presence of a boundary layer subsidence inversion.[11] The atmosphere is close to saturation below the inversion. A thin stratus cloud is present just at the base of the inversion. The dew point temperature sharply drops across the inversion and there is low relative humidity at higher altitudes. On account of this the water vapor content in the atmosphere above the inversion could be significantly reduced. This leads to a substantial decrease in the total water vapor content in the atmosphere and hence to reduced water vapor absorption. The CO_2 distribution in the atmosphere, however, is unaffected by the inversion. Under these conditions of vertical stratification, $\bar{T}$ can differ significantly for CO_2 as compared to water vapor. The effective altitude of $\bar{T}$

is closer to the sea surface in the presence of inversion for water vapor, while for CO_2 the altitude of $\bar{T}$ in the atmosphere is relatively unaffected. For these two reasons, (level of $\bar{T}$ and amount of absorption), the contribution made by water vapor to $(\delta T)_B$ [Eq. (6)] can be less than that due to CO_2 in region B. In addition under these conditions it is possible to have $(\delta T)_A < (\delta T)_B$. This is observed in the IRIS data over regions of the oceans that have subsidence.

In order to appreciate the signal strength associated with the spectral features in regions A and B, as an example, we will make a rough estimate of $(\delta T)_A$ from the theoretical framework presented above [see Eq. (6)]. The water vapor spectral absorption, for a total of 1.5 g/cm^2, in region A is about 0.15. Now if we take the scale height for water vapor to be about 3 km we get $(T_s - \bar{T}) \simeq 10$ K and thus $(\delta T)_A \simeq 1.5$ K. This estimate does not take into account the water vapor continuum absorption. Inclusion of the continuum absorption reduces the radiance in the narrow windows of the spectral region more than that in the absorption centers. Thus the value of $(\delta T)_A$ given above is only a rough estimate and is very likely an overestimation.

RESULTS

With the help of the data from the IRIS instrument, which had a field of view of 100 km, we have inferred the presence of boundary layer stratus over global oceans on a seasonal basis. IRIS is a non-scanning device that was flown on *Nimbus 4* polar orbiting satellite. For this reason it yielded a limited number of observations. Typically there are some 20 observations in a grid box of 2° lat × 3° long during a period of 3 months. From these observations we have deduced the cases that show $(\delta T)_A < (\delta T)_B$.

In order to demonstrate such spectral details with the help of IRIS data we have selected two regions: 20–26°N and 125–140°W, and 15–25°S and 85–130°W. These are subtropical subsidence regions over the oceans. In Tables 2 and 3 we have listed several brightness temperature details pertaining to the IRIS spectral measurements in these subsidence regions for the period June, July and August 1970. These details are brightness temperature at 900 cm^{-1} (11 μm), number of observations where $(\delta T)_A < (\delta T)_B$, $(\delta T)_A$, $(\delta T)_B$, and $(\delta T)_B - (\delta T)_A$. Also, we have included total numbers of observations in column 6 of the Tables 2 and 3.

As shown in the tables the window temperature T_{11} varies from about 292 to 279 K. The warmest window temperatures given in the tables are within a few degrees of the sea surface temperature. The lowest value of T_{11} chosen is 279 K because the frequency of observations for $T_{11} < 279$ K decreases sharply. We find there are less than 4% of the total number of observations showing $T_{11} < 279$ K and so they are deleted from the tables. These two limiting temperatures 292 K and 279 K suggest that the clouds in these oceanic regions are generally within about 2 km above the sea surface. The reason for the variation in T_{11} in these observations we believe is primarily due to the cloud fraction. When the cloud fraction is small T_{11} is closer to the sea surface temperature, and when the cloud cover is nearly complete T_{11} is closer to 279 K.

All the information, including T_{11}, given in the tables suggests that there exist substantial numbers of observations which correspond to low altitude stratus clouds underneath the boundary layer inversion produced by pronounced subsidence. The cumulative frequency of occurrence of such stratus is about 50% of the total number of observations in the north Pacific subtropical region

Table 2. Spectral information pertaining to the stratus clouds linked to strong subsidence inversion over the subtropical north Pacific 20–26°N and 125–140°W during June, July, and August 1970. Total number of observations and number with $\delta T_B > \delta T_A$.

Window temp (K) T_{11}	When $\delta T_B > \delta T_A$ (K)				Total frequency of obs.
	Frequency	δT_A	δT_B	$\delta T_B - \delta T_A$	
291 ± 1	1	0.528	0.930	0.412	21
289 ± 1	8	0.734	0.888	0.154	45
287 ± 1	16	0.470	0.659	0.189	74
285 ± 1	50	0.340	0.555	0.215	96
283 ± 1	49	0.116	0.374	0.258	69
281 ± 1	37	0.042	0.329	0.287	64
279 ± 1	19	0.021	0.361	0.340	39

Table 3. Spectral information pertaining to the stratus clouds linked to strong subsidence inversion over the subtropical south Pacific 15–25°S and 85–130°W during June, July, and August 1970. Total number of observations and number with $\delta T_B > \delta T_A$.

Window temp (K) T_{11}	When $\delta T_B > \delta T_A$ (K)				Total frequency of obs.
	Frequency	δT_A	δT_B	$\delta T_B - \delta T_A$	
293 ± 1	14	1.111	1.230	0.119	134
291 ± 1	20	0.926	1.085	0.159	278
289 ± 1	36	0.771	0.912	0.141	297
287 ± 1	69	0.677	0.827	0.150	301
285 ± 1	61	0.529	0.725	0.196	205
283 ± 1	56	0.333	0.582	0.249	146
281 ± 1	69	0.150	0.420	0.270	119
279 ± 1	43	0.012	0.278	0.266	104

to the west of California. Over the subtropical south Pacific to the west of Peru the occurrence of these stratus clouds with $(\delta T)_A < (\delta T)_B$ is less frequent probably due to weaker subsidence. The order of magnitude of $(\delta T)_A$ is about 1 K as estimated in the previous section. Furthermore, as T_{11} decreases we note $[(\delta T)_B - (\delta T)_A]$ increases. The corresponding $(\delta T)_A$ and $(\delta T)_B$ values suggest that strong subsidence reduces water vapor content in the atmosphere and thereby $(\delta T)_A$ more rapidly than $(\delta T)_B$. This is apparently a consequence of the hot band of CO_2 which is present in $(\delta T)_B$.

Based on the analysis presented above and the IRIS data we have produced a map of the frequency of stratus associated with pronounced subsidence over the Pacific ocean 150°E–80°W and 50°N–50°S for the season June, July, August of 1970. The data are shown in grids of 2° lat × 3° long in Fig. 5. The contours in Fig. 5 reveal significant frequency of occurrence of such stratus clouds over the subtropical subsidence regions particularly near the eastern sections. We note the lack of such clouds over the Intertropical Convergence Zone (ITCZ) and over the South Pacific Convergence Zone (SPCZ).

CONCLUSIONS

Identification of the cloud type with spectral information can be valuable in weather and climate studies. Analyses made on a large scale with satellite images of the clouds in the visible region tend to be subjective in discriminating different cloud types.[12] Infrared brightness temperature measurements in broad bands around 11 and 6.7 μm obtained from space-borne radiometers, GOES and METEOSAT, for example, have similar limitation. The spectral method presented here to identify the boundary layer stratus can supplement these existing methods.

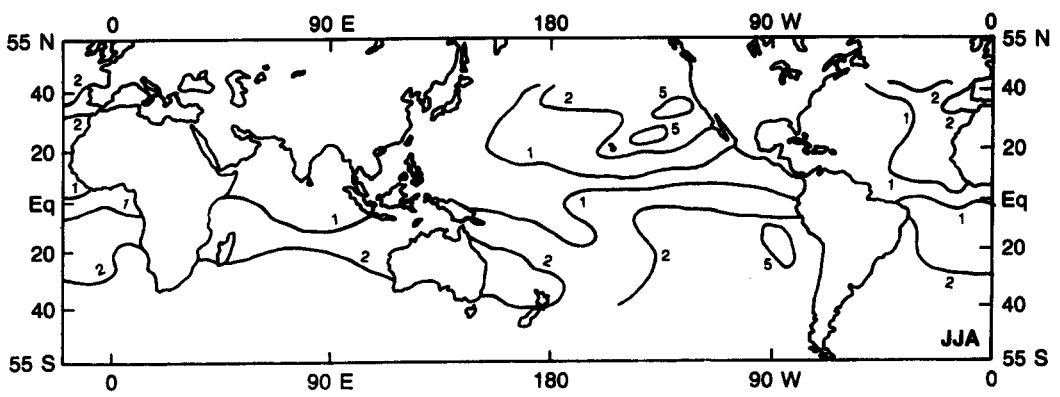

Fig. 5. The frequency of observation (when $T_{11\,\mu m} > 285$ K) showing the spectral signature associated with the boundary layer stratus clouds produced by strong subsidence ($\delta T_A < \delta T_B$ as discussed in the text). Land and islands are shown by the symbol @.

To implement this method spectral resolution of about 3 cm^{-1} with a moderate spatial resolution and a relative accuracy of ~ 0.2 K are needed. At present these requirements could be readily achieved.

The method developed here to identify stratus clouds may not work over cold oceans where the atmospheric water vapor content is less than about 1.5 g/cm^2. On this basis we estimate the sea surface temperature should be in excess of 280 K for the method to work. This limits the applicability of this method to latitudinal region between $\sim 50°$N and 50°S. Based on this study we believe it will be useful to have i.r. spectral measurements, of the kind described here, in aircraft experimental programs such as FIRE that are meant to investigate the stratus clouds.

We had shown in earlier studies,[8,9] with the help of the IRIS data, the large scale distribution of high altitude thin cirrus clouds associated with convective motions over the warm oceans. This study helps us to get the distribution of stratus clouds associated with subsidence. Since it is natural to expect a connection between the rising convective motions and the subsidence, long term study of these two cloud systems with the help of the satellite data can be valuable in the investigation of global change and greenhouse warming.

REFERENCES

1. K. N. Liou, *An Introduction to Atmospheric Radiation*, Academic Press, New York, NY (1980).
2. C. M. R. Platt and G. L. Stephens, *J. Atmos. Sci.* **37**, 2314 (1980).
3. W. B. Rossow, L. C. Garder, P. Lu, and A. Walker, *International Satellite Cloud Climatology Project (ISCCP), Documentation of cloud data WMO/TD*-No. 266, World Meteorological Organization, Geneva (1991).
4. L. L. Stowe, C. G. Wellemeyer, T. F. Eck, H. Y. M. Yeh, and the *Nimbus-7* Cloud Data Processing Team, *J. Climate* **1**, 445 (1988).
5. L. L. Stowe, H. Y. M. Yeh, C. G. Wellemeyer, H. L. Kyle, and the *Nimbus-7* Cloud Data Processing Team, *J. Climate* **2**, 671 (1989).
6. G. Yamamoto, M. Tanaka, and S. Asano, *J. Atmos. Sci.* **27**, 282 (1970).
7. G. W. Paltridge and C. M. R. Platt, *Radiative Transfer Processes in Meteorology and Climatology*, Elsevier, New York, NY (1976).
8. C. Prabhakara, R. S. Fraser, G. Dalu, M.-L. C. Wu, R. J. Curran, and T. L. Styles, *J. Appl. Met.* **27**, 379 (1988).
9. C. Prabhakara, D. P. Kratz, J.-M. Yoo, G. Dalu, and A. Vernekar, *JQSRT* (1993).
10. D. P. Kratz, B.-C. Gao, and J. T. Kiehl, *J. Geophys. Res.* **96**, 9021 (1991).
11. H. Riehl, *Tropical Meteorology*, McGraw–Hill, New York, NY (1954).
12. P. F. Clapp, *Mon. Weath. Rev.* **92**, 495 (1964).